Experimental Thermal and Fluid Science 130 (2022) 110457

Contents lists available at ScienceDirect

Experimental Thermal and Fluid Science

journal homepage: www.elsevier.com/locate/etfs

Aspect ratio and the dynamic wake of the Ahmed body

James Venning [a,*], Thomas McQueen [a], David Lo Jacono [a,c], David Burton [b], Mark Thompson [a], John Sheridan [a]

[a] Fluids Laboratory for Aeronautical and Industrial Research (FLAIR), Monash University, Clayton, VIC 3800, Australia
[b] Monash Wind Tunnel Research Platform, Department of Mechanical and Aerospace Engineering, Monash University, Clayton, VIC 3800, Australia
[c] Institut de Mécanique des Fluides de Toulouse (IMFT), CNRS, UPS, Université de Toulouse, Allée Camille Soula, F-31400 Toulouse, France

ARTICLE INFO

Keywords:
Ahmed body
Trailing vortices
Aspect ratio
Time-resolved PIV
Spectral POD

ABSTRACT

The dynamic structures in the wake of the Ahmed body with a 25° slant angle were investigated. It is well established that the wake is dominated by two, counter rotating, streamwise vortex structures (C-pillar vortices). The influence these vortices have on the flow over the slant back was altered by modifying the width of the body between 60% to 120% of the standard width. The wake was measured using time-resolved particle-image velocimetry in several streamwise and spanwise planes for a height-based Reynolds number of 2.6×10^4. The wake measurements were decomposed with a spectral proper orthogonal decomposition technique, revealing two oscillatory modes. Firstly, the C-pillar vortical structures alternately contract and expand with a Strouhal number of 0.24, mildly dependent on the width. Secondly, the boundary layers on the sides of the body separate at the end of the body, forming shear layers with a dominant frequency of $St = 2.30$. Reducing the width of the body to 60% rotates the symmetry axis of the shedding mode. Furthermore, changing the spacing between the C-pillar vortices, by changing the width of the body, alters the nature of the spanwise vortical structures that form behind the base of the model. Intermediate width bodies produce two stable spanwise vortices. For wide bodies, the flow remains separated over the entire slant, and the top spanwise vortex does not form. Rather, the flow over the slant resembles a free shear layer with a Kelvin–Helmholtz-like instability leading to periodic shedding of small-scale vortex structures. Conversely, for narrow bodies, this phenomenon is observed at the bottom of the body and the lower spanwise vortex no longer forms while the flow over the slant remains attached.

1. Introduction

The Ahmed geometry [1] has been studied in depth over the last four decades as a shape generalising the flow features of an automobile. A vast quantity of literature, both experimental and computational, has been produced with respect to the effect that slant angle has on the wake and hence the body forces. The majority of these studies are focused on the time-averaged wake, which is helpful to an extent, but can be deceptive as the time-averaged flow can hide temporally-varying features [9,16] or produce unphysical results. Studying the instantaneous flow is of importance in understanding the physical mechanisms at play. This in turn is essential to tackling the problem of active flow control, which has been shown as an effective method to influence the drag force on this body [see 4, for a relevant review].

The major time-averaged structures in the wake of this geometry have been defined by Ahmed et al. [1] (Fig. 1). They consist of a pair of vortices formed as the flow separates at the rear of the model (labelled A and B for the top and bottom vortices, respectively) which are tilted downstream [36]. The dominant flow feature is a pair of streamwise vortices (labelled C) that are formed as the flow in the side boundary layers rolls over the slant edge. These counter-rotating, streamwise vortices are often termed the 'C-pillar' vortices.

While there is agreement in the literature regarding the dominant time-averaged flow structures present, there is significant scatter in results for the wake dynamics. Part of this scatter may be ascribed to the fact that, predominantly, point measurements have been used to probe the wake around the body at a few select locations, often specific to individual studies. In particular, coherent frequencies have been identified at the front of the body [23], above the roof [41], over the slant [21,23,29,30,20,38,41], and in several locations behind the base [37,23,20,22,32,39,41,16,40].

In an attempt to reconcile the scatter observed in the dynamic data,

* Corresponding author.
E-mail address: mail@jamesvenning.net (J. Venning).

https://doi.org/10.1016/j.expthermflusci.2021.110457
Received 30 September 2020; Received in revised form 25 May 2021; Accepted 3 June 2021
Available online 2 July 2021

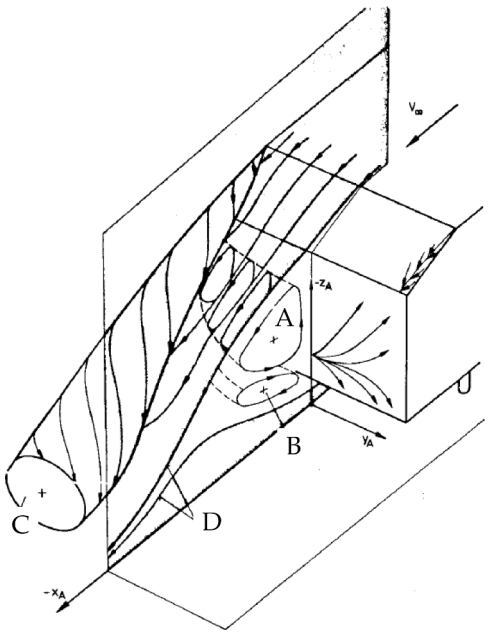

Fig. 1. Time-averaged structures in the wake of the Ahmed body after Ahmed et al. [1].

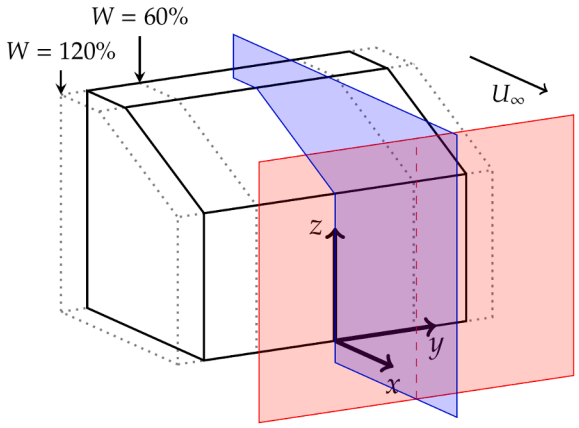

Fig. 2. Rear of the Ahmed body with PIV planes and coordinate system. The origin is at the base of the rear surface of the model, in the symmetry plane. The cross-stream plane (yz) is shown in red at a location of $x/L = 0.2$, the xz symmetry plane is in blue. The narrowest (60%) and widest (120%) bodies are indicated with the dotted lines.

Zhang et al. [41] conducted a comprehensive hot-wire study accompanied by flow visualisation and non-time-resolved PIV. They used a hot-wire analysis to identify seven important frequencies and the origin of each. They identified two frequencies above the roof emanating from separation near the front of the body, two over the slant associated with the separated shear-layer and hairpin vortices that form, two originating from the upstream and downstream struts, and lastly, a single frequency associated with the recirculating bubbles behind the base. They also provided a conceptual model of the flow structures associated with these frequencies. However, the point measurements from the hot-wire analysis are uncorrelated in space and so the structure of these dynamic systems can only be inferred. In this study, we provide the dominant Strouhal numbers across the wake, downstream of the body, and additionally give visualisations to aid in the understanding of the wake dynamics.

While Zhang et al. [41] did not discuss any significant periodic movement of the dominant C-pillar vortices, distinct dynamic modes of similar large-scale streamwise vortex structures have been identified in the wake of a high-speed train – a comparable bluff-body ground vehicle geometry. Bell et al. [6] identified a cyclic process whereby one vortex grows in size and moves upwards and outwards, while the other reduces in size and moves downwards and inwards.

While the Reynolds number of the present study is orders of magnitude smaller than that of road vehicles, the time-averaged large-scale structures have been shown to compare well for Reynolds numbers up to at least 0.2×10^6 [see, for example 10,25,27]. Some effects of the Reynolds number will be evident when comparing these results to full scale, for example, the streamwise diffusion of vorticity and the size of any recirculation regions, however, the flapping mechanism is expected to be more dependent on the geometry rather than the Reynolds number [see, for example, 3, who show the wake topology behind an estate vehicle at low Reynolds number to be qualitatively similar to that at high Reynolds number, both in terms of time-averaged and instantaneous features]. The attachment state of the flow over the rear slant is determined by a coupling of the Reynolds number, the slant angle, and the aspect ratio. The effect of the Reynolds number on various shedding frequencies has been investigated by Zhang et al. [41]. For the base-pressure mode which is of the most relevance here, they have shown the frequency to initially increase as the size of the recirculation bubble decreases, before asymptoting. No changes in the shedding physics for this mode were noted in that study.

For a three-dimensional geometry such as a finite-width flat plate or cylinder, the aspect ratio (span to chord or diameter) has been shown to be an important parameter in determining the flow state [e.g. 28,19] and controlling the interaction of vortices from different edges. The aspect ratio is an important scaling parameter for other geometries, such as insect wings [18,7], square and circular plates [12]. Grandemange et al. [15] showed that the low-frequency bistability for the square-backed Ahmed body was also dependent on the aspect ratio. For the slanted Ahmed body, the effect of aspect ratio has been studied for the time-averaged wake [35,8] showing a coupling between the aspect ratio and the slant angle to determine the flow state. There exists a critical combination of slant angle and aspect ratio which determines if the flow reattaches over the slant, driven by the additional downwash of the C-pillar vortices. While Venning et al. [35] showed the influence of aspect ratio on the time-averaged structures, the natural question arises regarding the influence of aspect ratio on the wake dynamics.

Much of the recent focus in this research space has been on the bi-stable nature of the square-back Ahmed model, which has been shown to exist in one of two asymmetric states [16,17,33,26]. This phenomenon is only observed in controlled laboratory environments, and the switching frequency between these is extremely low such that this is unlikely to be relevant to practical, full-scale vehicle aerodynamics.

While previous studies have provided the location of dominant Strouhal numbers in relation to the body, as discussed, their association with flow structures is often only inferred. This investigation focuses on the wake of the Ahmed body and aims to reveal the specific flow structures associated with dominant shedding modes and the variation of these structures with aspect ratio. We present a detailed analysis of the dynamics of the major structures in the wake using time-resolved particle image velocimetry (TR-PIV) and associated modal decompositions. By investigating the effect of changing body geometry on dominant Strouhal numbers, we show how the time varying structures are influenced by the relative strength of the C-pillar vortices. The paper is structured as follows: firstly, the details regarding the experimental setup are shown along with the modal decomposition tool. Secondly, the results of the standard-width Ahmed model are described. Thirdly, the effect of the aspect ratio on the dynamics is discussed, including a discussion on the time-varying nature of the A- and B- spanwise vortical structures. The paper concludes with a summary of the key findings.

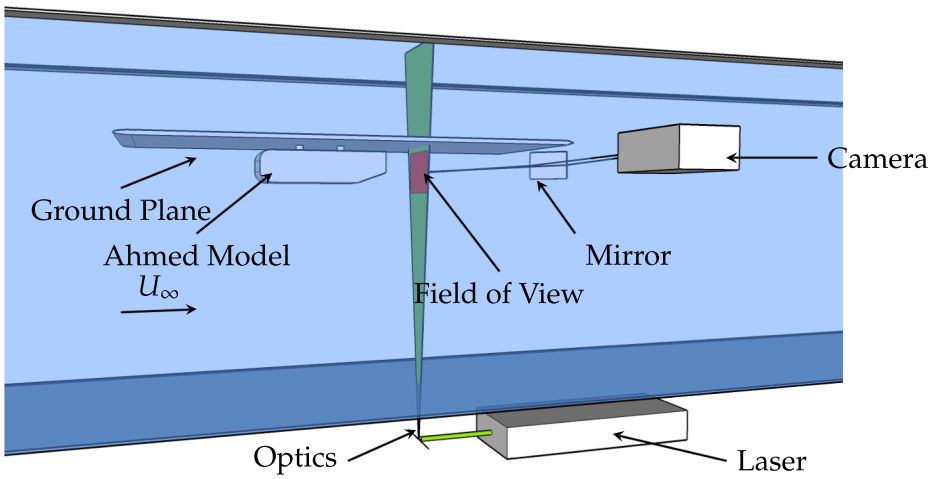

Fig. 3. Experimental setup for the cross-stream PIV acquisition.

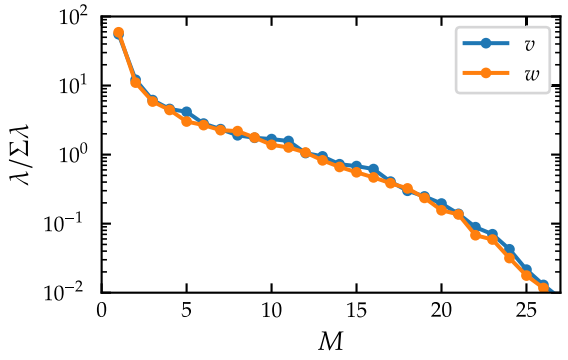

Fig. 4. Eigenvalues of the dominant shedding frequency behind the standard-width Ahmed body at $x/L = 0.2$. The horizontal (blue) and vertical (orange) velocity components are included. The values are represented as a ratio of the total, to indicate how much of the total variance is included in each mode.

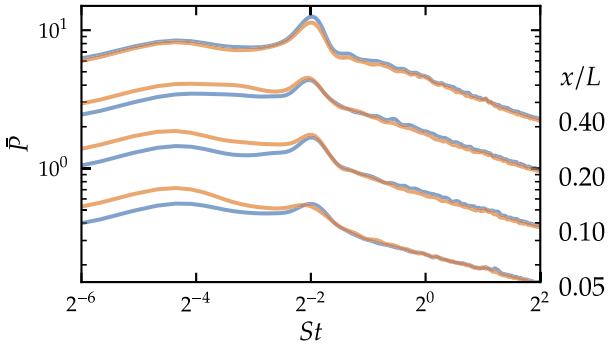

Fig. 5. Spatial average of the power spectral densities of the spanwise (blue) and vertical (orange) velocity fluctuations in the wake behind the standard-width Ahmed body at various downstream positions (offset vertically). The dominant peak is at $St = 0.24$ (based on height) for all downstream positions and corresponds to the flapping oscillations of the large structures. Closest to the body (lowest plot), there is a slight second peak at $St = 2.4$ corresponding to the shear layer fluctuations.

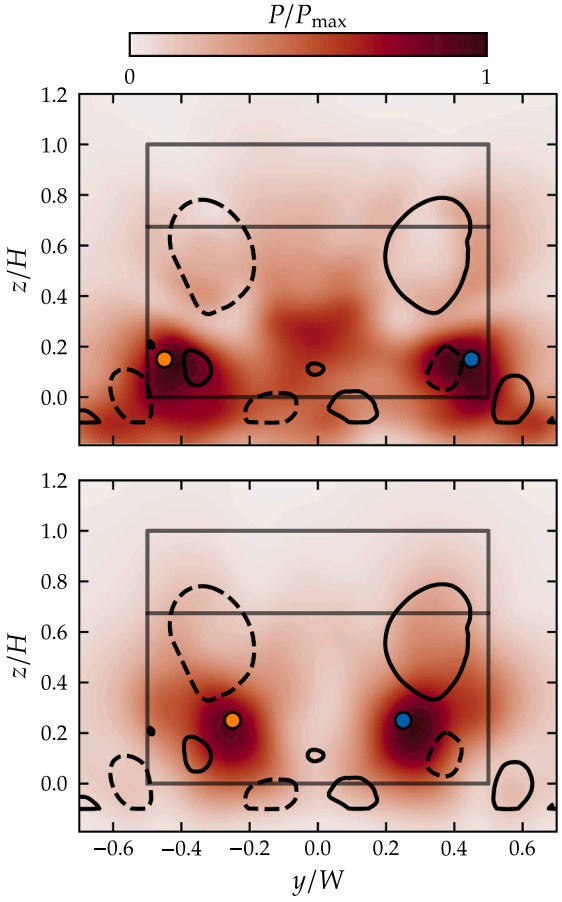

Fig. 6. Power of the $St = 0.24$ frequency across the cross-stream plane at $x/L = 0.2$. Top figure is for the spanwise fluctuations (v) while the bottom figure is the vertical fluctuations (w). The time-averaged vortex bounds $\Gamma_2 = \pm 2/\pi$ are shown with contours for reference (dashed indicates negative rotation). The markers indicate the locations for the time series in Fig. 7.

2. Experimental setup

The investigation was conducted in the recirculating free-surface water channel of the Fluids Laboratory for Aeronautical and Industrial Research (FLAIR) at Monash University. The water channel has a working section of 600 mm in width, 800 mm in depth and 4000 mm in length. The free-stream turbulence level is less than 1% at the free-stream speed investigated. Four Ahmed bodies were manufactured out of Acetal at one-quarter geometric scale of the original study by Ahmed et al. [1]. The widths of each body varied between 60% and 120% of the standard width (Fig. 2) in order to investigate the sensitivity of the wake dynamics to the aspect ratio of the body. The radii on the front end were

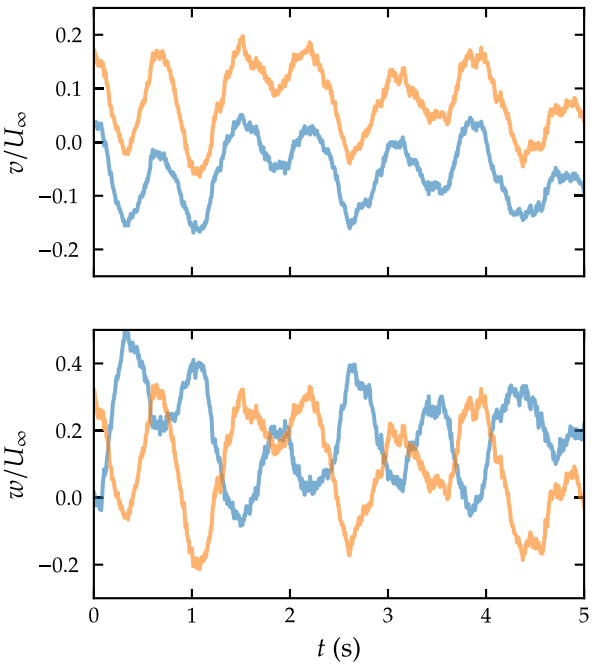

Fig. 7. POD-filtered timeseries at symmetric positions downstream of the Ahmed body at $x/L = 0.2$. Top is spanwise velocity at $y/W = \pm 0.45$, $z/H = 0.15$. Bottom is vertical velocity at $y/W = \pm 0.25$, $z/H = 0.25$. The blue timeseries is for positive y/W positions, and the orange is for negative. The locations for the time series are indicated by markers in Fig. 6. (For interpretation of the references to colour in this figure legend, the reader is referred to the web version of this article.)

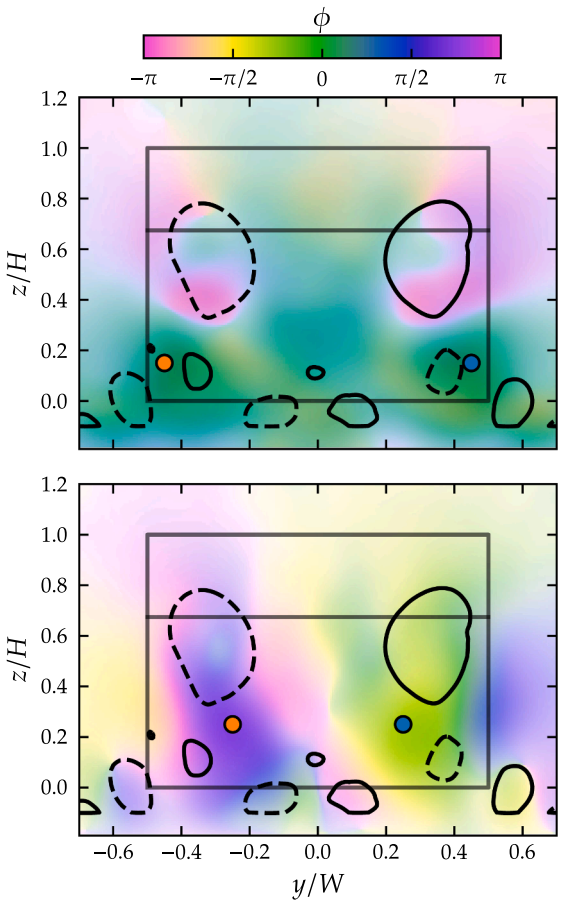

Fig. 8. Phase of the first mode from the SVD decomposition of the $St = 0.24$ frequency across the cross-stream plane at $x/L = 0.2$. Top figure is for the spanwise fluctuations while bottom figure is the vertical fluctuations. The time-averaged vortex bounds $\Gamma_2 = \pm 2/\pi$ are shown with contours for reference (dashed indicates negative rotation). The markers indicate the locations for the time series in Fig. 7.

kept constant at 25 mm (26% of the standard body's width) for each body. Researchers have used various mounting configurations in previous studies including: four airfoil struts [2]; the omission of struts altogether for numerical studies [21]; four cylindrical struts [1], which is the most common; or even no gap at all [40]. In this study, the bodies were attached to a ground-plane through two symmetric airfoils mounted on the model centre-line. This mounting configuration was used to enable drag measurements for a separate study. The ground plane, similar to that employed in previous studies [29], enabled the generation of a thin boundary layer at the model. The ground plane had a 4:1 elliptical leading edge and extended $4.2H$ (body heights) upstream of the model. The freestream velocity was set to 0.37 m/s and the Reynolds number based on the height of the body was 2.6×10^4. This setup has been validated for previous Ahmed body studies [35].

The TR-PIV system utilised a PCO Dimax S4 camera recording at 200 fps with resolution 2016 px × 1504 px. The camera imaged particles (Vestosint, Germany) of mean diameter 56 μm and density 1.016 g/cm^3 suspended in the flow and illuminated with a 5 W continuous wave laser (CNI, China). The laser produced a continuous 3 mm diameter beam at 532 nm wavelength, which was directed through a planar-convex lens to split the beam into a 3 mm thick sheet.

The images were analysed using in-house cross-correlation software [13,24] with a final window size of 32 × 32 pixels and a 75% overlap. For the cross-stream (yz) plane, the resultant vector fields contained $N_y = 249$ and $N_z = 185$ vectors. With a magnification factor of 13.1 px/mm, the field of view was $2.1W \times 1.6H$ and the vector pitch was 0.6mm ($0.008H$). The streamwise (xz) plane had a magnification factor of 8.9 px/mm, and the field of view was $0.9L \times 2.0H$ with a vector pitch of 0.9 mm. The uncertainty on the PIV measurements is approximately 1.5 mm/s which corresponds to about 0.4% of the freestream velocity.

The cross-stream planes downstream of the model were acquired by using a 45° mirror in the flow to allow imaging orthogonal to the yz laser plane (Fig. 3). Care was taken to ensure minimal influence of the flow near the body [verified in 34]. For each downstream plane, located at $x/L = 0.05$, 0.1, 0.2, and 0.4, 8000 images were acquired at a sampling frequency of 200 fps, corresponding to more than 30 cycles of the dominant frequency. The maximum resolvable frequency is the Nyquist frequency of 100 Hz, which is a height-based Strouhal number of 20. For the streamwise planes, the camera was placed orthogonal to the imaging plane.

The velocity time-series in this paper have been filtered with a proper orthogonal decomposition (POD) in order to extract the motions of only the larger-scale features in the wake. The data was first decomposed into orthogonal modes based on the energy of each mode. By reconstructing the data onto a smaller subset of these modes, PIV error and small scale fluctuations can be reduced [11]. Data processed this way are labelled in the captions as 'POD filtered'.

2.1. Spectral estimation

The global modes are visualised using a methodology similar to [5], but using an additional decomposition, similar to the spectral POD presented in Towne et al. [31]. A Fast Fourier Transform (FFT) is applied to the velocity data at every location in the spatial domain. This transform allows the dynamics at any one point to be investigated, as well as how the amplitude and phase of any frequency varies across space. A Welch periodogram with Hanning windows was used to investigate how these frequencies varied in time as well. For each data set, the window length N was 1024 points, representing 5.12 s or approximately 6 cycles

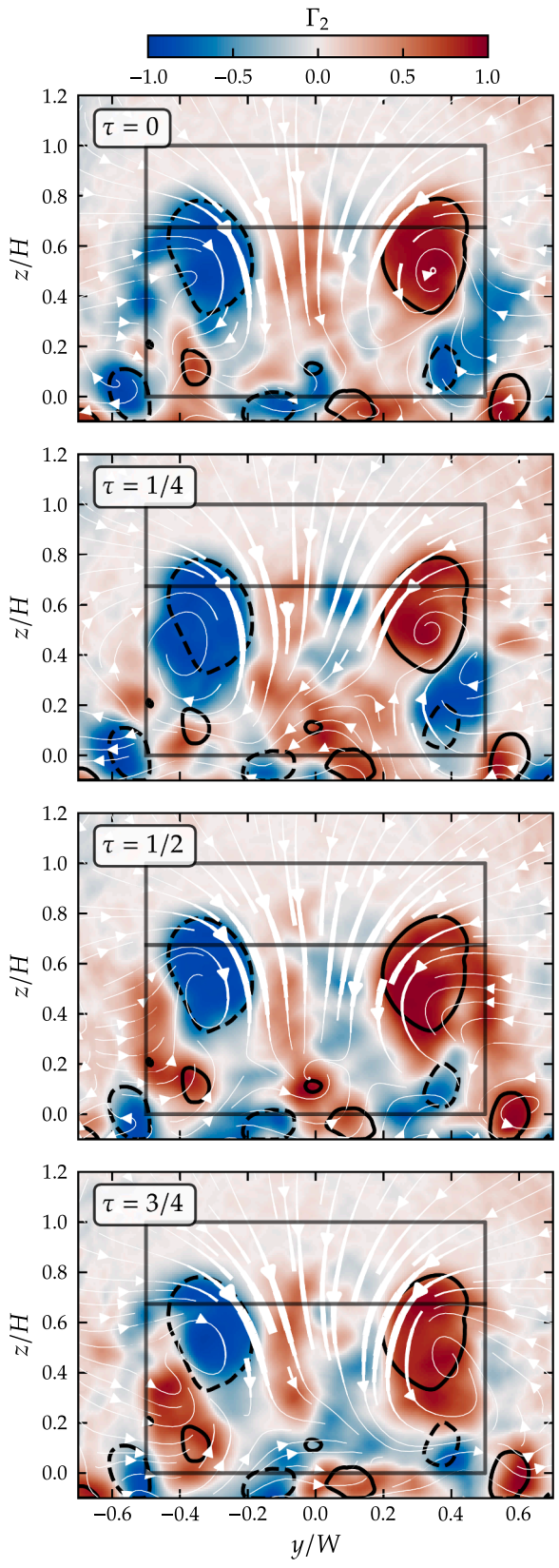

Fig. 9. Phase-averaged velocity (white) and filled contours of Γ_2 at four positions in the cycle (τ). The downstream position is $x/L = 0.2$ and the line weight is proportional to the local velocity magnitude. Black contours represent the time-averaged flow structures (Γ_2=±2/π). Flow is towards the observer.

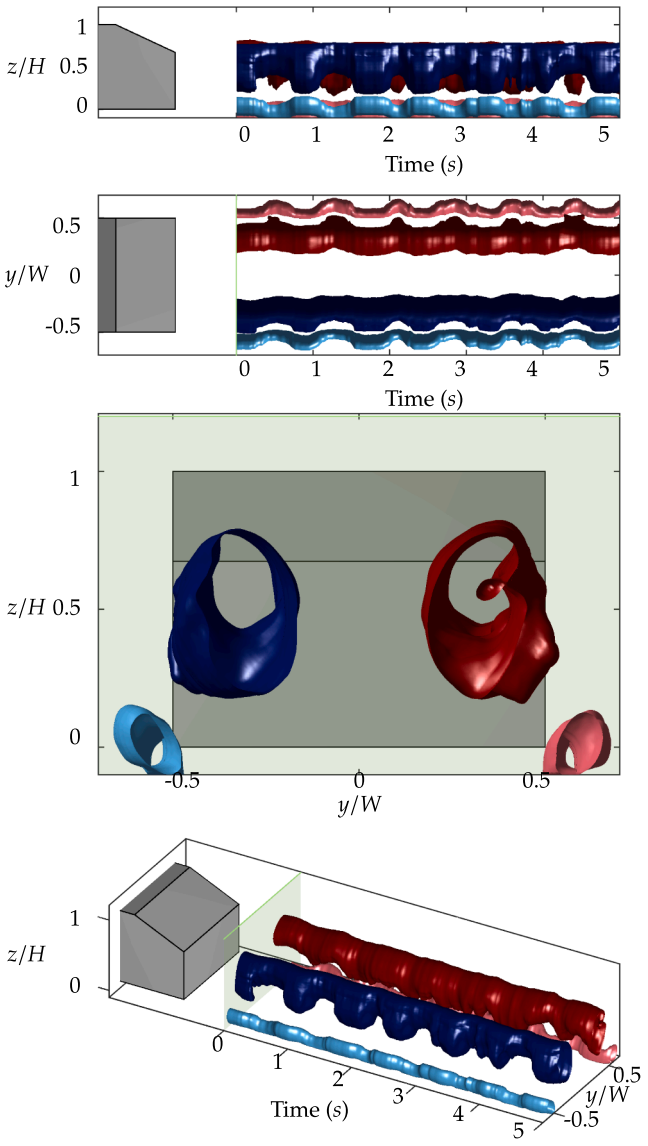

Fig. 10. Cross-stream dynamics at $x/L = 0.2$ showing motion of the C-pillar and corner vortices over a five second period. In order from top down: side view, top view, rear view, and isometric view. The green plane represents the relative location of the acquisition plane to the Ahmed body. Positively rotating structures in reds and negatively rotating structures in blues. The C-pillar vortices are the darker structures, the lighter structures are the corner vortices. (For interpretation of the references to colour in this figure legend, the reader is referred to the web version of this article.)

of the dominant frequency. The shift between windows N_S was 256 points. Given the time sequence is 8000 points, there are 35 windows (T).

For each spatial location (j), and each window (t), the FFT of a velocity signal (x_n) is given by Eq. 1 with P and ϕ corresponding to the power and phase of each sinusoidal component of the time series, and k is the wavenumber.

$$X_{jtk} = \mathscr{F}\left(x_{jtk}\right) = \sum_{n=0}^{N-1} x_n e^{-2\pi i k n/N} \tag{1a}$$

$$P_{jtk} = \sqrt{\mathrm{Re}\left(X_{jtk}\right)^2 + \mathrm{Im}\left(X_{jtk}\right)^2} \tag{1b}$$

$$\phi_{jtk} = \mathrm{Arg}\left(X_{jtk}\right), \tag{1c}$$

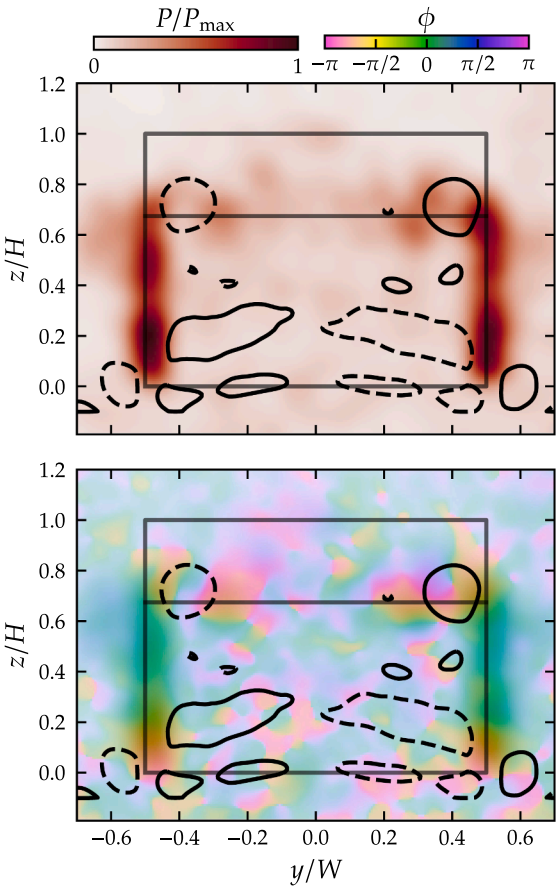

Fig. 11. Power (top) and phase (bottom) of the $St = 2.30$ mode of the spanwise velocity fluctuations across the cross-stream plane at $x/L = 0.05$. The time-averaged vortex bounds $\Gamma_2 = \pm 2/\pi$ are shown with contours for reference (dashed indicates negative rotation).

where $\mathrm{Arg}(X_{jtk})$ represents the principal value of the angle from the real axis to a line from the origin to the complex number X_{jtk}, which, in a practical sense, is $\mathrm{atan2}\big(\mathrm{Im}(X_{jtk}), \mathrm{Re}(X_{jtk})\big)$.

The averaging across the N_w windows is straightforward for the power:

$$\overline{P_{jk}} = \frac{1}{N_w} \sum_{t=1}^{N_w} P_{jtk} \tag{2}$$

However, because the phase angle is constantly changing, a temporal average of ϕ_{jtk} will not provide a representative view of the phase, in fact, given enough t instances, the temporal average will be zero. Thus, the singular value decomposition (SVD) was used to decompose the Fourier coefficients and return a series of eigenmodes, the first being most representative of the phase mode. The SVD factorizes the complex field $\mathbf{\Phi}$ (a matrix in which each column represents a different window (t) of the phase of one frequency (ϕ_k) – the size of this matrix is $N_y N_z \times N_w$), decomposing it with:

$$\mathbf{\Phi} = L \Sigma R \tag{3}$$

Which returns:

- $\mathbf{L}$: a series of orthonormal eigenvectors of $\mathbf{\Phi}\mathbf{\Phi}^T$; a square matrix with $N_y \cdot N_z$ columns
- $\mathbf{\Sigma}$: N_w eigenvalues corresponding to how much of the variability in $\mathbf{\Phi}$ is accounted for in each mode, and
- $\mathbf{R}$: a series of eigenvectors of $\mathbf{\Phi}^T\mathbf{\Phi}$; a square matrix of size $N_w \times N_w$

The N_w global modes are thus the projections of $\mathbf{\Phi}$ onto the basis eigenvectors, which are then normalized to provide meaningful values of the magnitude:

$$\frac{\mathbf{\Phi} \times R}{||\mathbf{\Phi} \times R||} \tag{4}$$

The variance is given by the eigenvalues in $\mathbf{\Sigma}$, which reflect how much of the total variance is contained in each mode. This is given for a typical case in Fig. 4. The first mode contains approximately 60% of the variance, with subsequent modes having at most 10% each. Since the first mode captures the majority of the variance, it is the only mode that will be presented throughout this manuscript for each of the cases. The higher order modes are corrections to this base mode.

This phase distribution for one frequency can then be plotted across the spatial domain. Because all the PIV measurements in one plane are simultaneous, the differences in phase across the domain is meaningful. There is no fixed zero-phase point, so the figures have an arbitrary reference. This means the phase differences between different bodies or different downstream positions are not meaningful.

3. Results

3.1. Cross-stream dynamics of the standard width Ahmed body

The velocity field in the cross-stream plane behind the standard-width body is first analysed. The spectra of the velocity fluctuations averaged over the yz plane at four streamwise positions are given in Fig. 5 for this body. The spatial average of the spectra is the average of the PSD from every velocity location in the yz plane. The spatial average is used here to highlight the dominant global modes, rather than any frequencies that are isolated in space. Both the vertical and spanwise velocity fluctuations show a distinct peak at $St = 0.24$, with the height used as the length-scale. The power of this peak indicates that this is the dominant motion for this specific body, wake location, and Reynolds number.

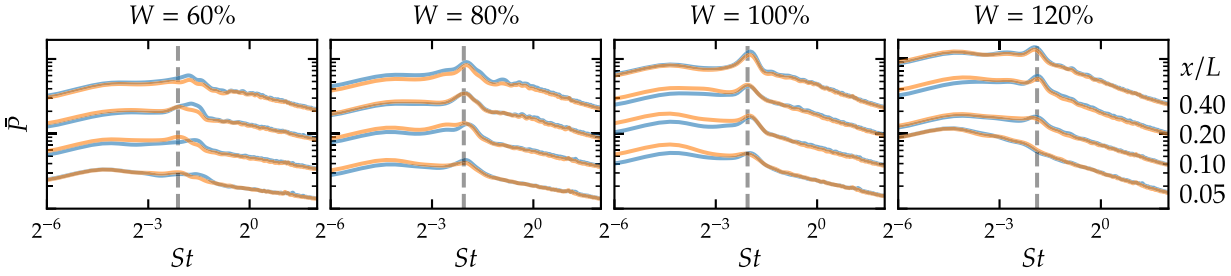

Fig. 12. Frequency spectra (arbitrary power units) for each of the Ahmed models tested in various cross-stream planes. The spanwise and vertical components are presented in blue and orange, respectively. The spectra at each downstream position has been shifted vertically for clarity, and is indicated on the right. The dominant shedding frequency is mildly dependent on the body width, and is indicated by vertical lines at $St = 0.23$, 0.24, 0.24, and 0.27 for the four bodies respectively.

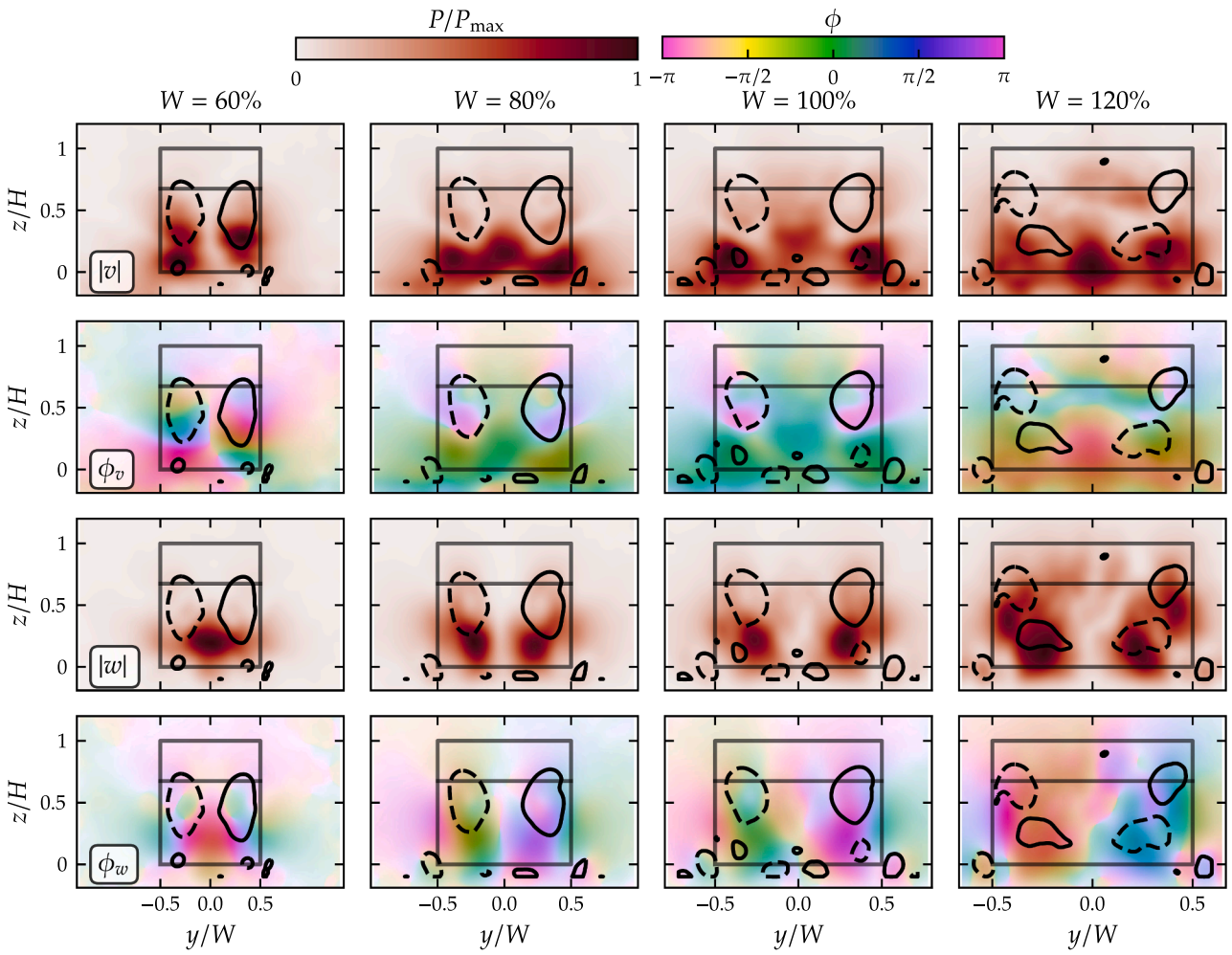

Fig. 13. Power and phase distributions behind the four Ahmed bodies for the dominant frequency. The four rows are: power distribution of the spanwise velocity, phase difference of the spanwise velocity, power distribution of the vertical velocity and the phase difference of the vertical velocity.

Fig. 6 shows the global mode, i.e. the spatial distribution, of the amplitude associated with the $St = 0.24$ frequency. For the spanwise fluctuations, v (top), this frequency is strong behind the lower corners of the body, as well as behind the center of the back surface. The time-averaged vortex bounds, given by contours of the Γ_2 criterion [14], are given in Fig. 6 to show the location of the major structures in the wake. Venning et al. [35] give the full spatial evolution of these time-averaged structures. Note that the corner vortices are likely to be stronger in this setup due to the lack of struts near the sides of the body. Fig. 6 (b) shows that the $St = 0.24$ frequency is also strong in the vertical fluctuations (w) just under and inside the C-pillar vortices.

Probing two points in these high-amplitude regions (indicated by the blue and orange circle markers in Fig. 6) reveals the scale and phase of the velocity fluctuations, and Fig. 7 gives the timeseries of the velocity signals at these symmetric locations. These timeseries have been filtered with the POD to remove the small-scale fluctuations and experimental noise. The spanwise velocity timeseries fluctuate in phase, while the vertical velocity fluctuates half a period out of phase. This phase shift can be quantified from the phase angle returned by the FFT (Eq. 1c). Fig. 8 is the first mode from the SVD on the phase data, showing that this pattern is consistent across the whole wake, with Fig. 8 (a) being symmetric about the $y/W = 0$ line, and Fig. 8 (b) being anti-symmetric about that line. Physically, the phase patterns depicted in Fig. 8 describe flow structures that are simultaneously moving in phase together in the spanwise direction (as a serpentine mode) while moving alternately in the vertical direction.

The TR-PIV instances were phase-averaged based on the dominant $St = 0.24$ frequency. The time-averages of each bin are plotted in Fig. 9. The lower part of each C-pillar vortex alternately moves downwards. At the same time, the corner vortex is pushed outboard and upwards, causing the spanwise velocity fluctuations seen in the lower corners of Fig. 6 (a). The top of the C-pillar vortex is stable in time due to the fixed location of the roll-up over the C-pillars. The streamwise element of the B-vortex, which sits below the C-pillar vortices, alternately grow and contract with the same period.

This motion can also be visualised through the use of a three-dimensional space–time plot. Here, the y and z axes of the plot correspond to the y and z spatial axes and the x axis of the plot denotes time. This shows how the structures vary in space, through time. The data is first filtered using a POD filter. The reconstruction is based on the three most energetic modes, which was found to reproduce the high-energy motions of the key structures without introducing the small-scale structures and error. Fig. 10 shows one such space–time plot, generated from TR-PIV data at $x/L = 0.2$. Time progresses to the right of each figure, except for the third figure, where time increases out of the page. The dominant frequency seen in the FFT analysis manifests itself in variations in the locations of the major structures. The only element of the flow structures depicted in Fig. 10 that does not vary significantly in time is the top of the C-pillar vortices, which remain stationary at $z/H = 0.75$. The bottom of the C-pillar vortex, on the other hand, strengthens and expands downwards and outwards. This occurs periodically (at $St = 0.24$) and when it occurs, the

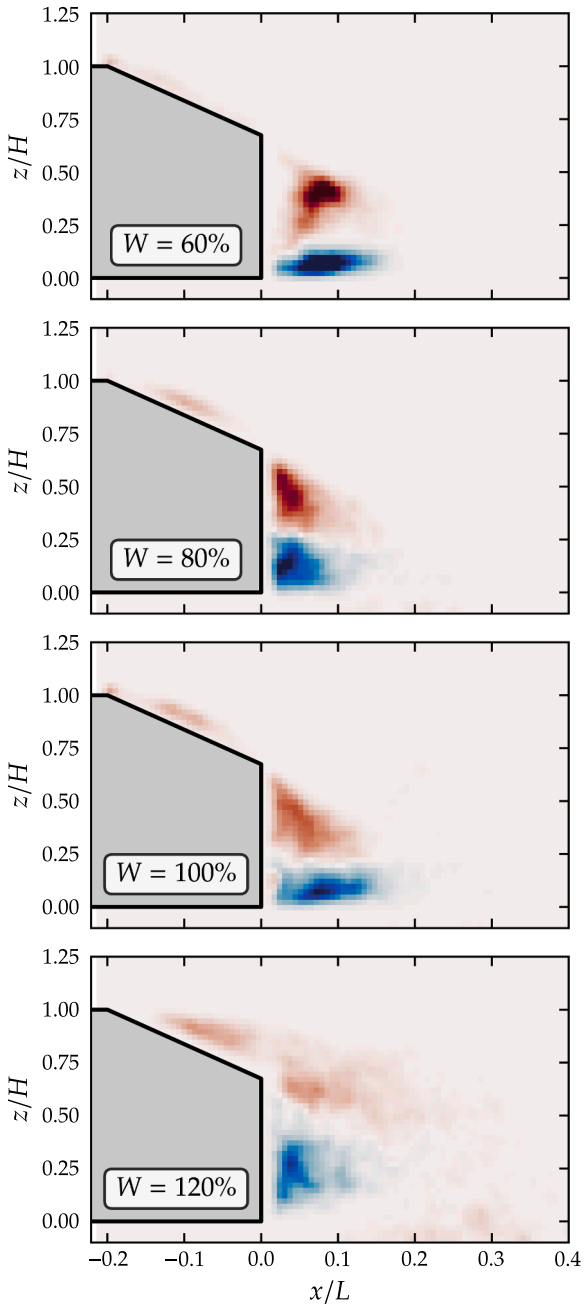

Fig. 14. Distribution of the locations of the maximum (red, clockwise) and minimum (blue, counter-clockwise) of the Γ_1 field at $y/W = 0$ highlighting the variation of the cores of the A- and B-vortices, respectively, as the aspect ratio is varied.

following happen:

- the base of the C-pillar vortex moves outboard,
- the corner vortex is shifted upwards and outboard,
- the opposite C-pillar vortex is contracted to its minimum extent,
- the opposite corner vortex is shifted downwards and inboard, and
- the streamwise element of recirculation region B is significantly strengthened below the opposite C-pillar vortex.

3.2. Shear-layer vortices

At the closest plane to the body ($x/L = 0.05$), the modal analysis detects the shear layer vortices emanating from the separated flow at the

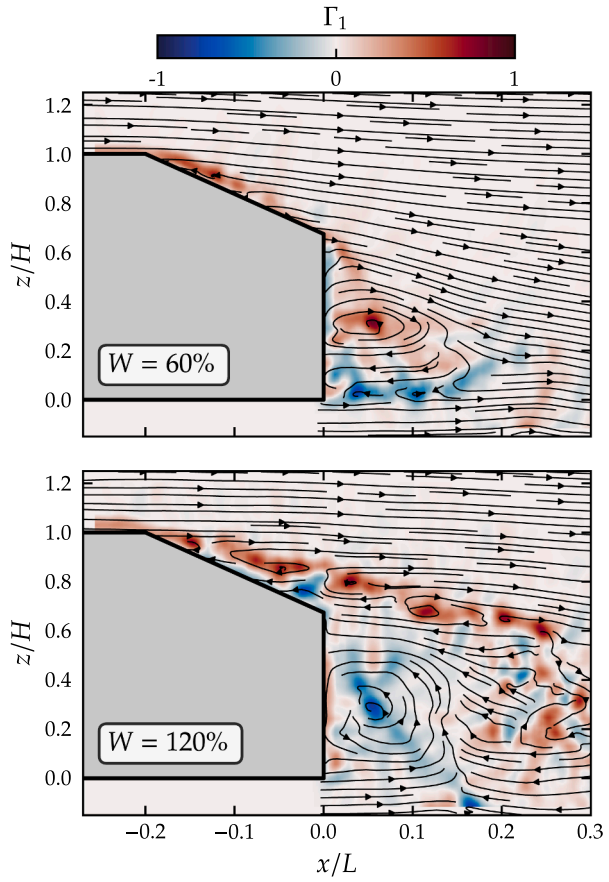

Fig. 15. Instantaneous wake of the 60% and 120% width models. Streamlines in black and contours of Γ_1 in colour with red indicating positive (clockwise) rotation and blue indicating negative (counter-clockwise) rotation. The overlaid streamlines are indicative of the local flow direction only.

sides of the body. These are seen in the spanwise component of the velocity, but not the vertical, since the vortices are oriented vertically. Fig. 11 shows the power and phase of this mode in the spanwise velocity. The energy is concentrated in line with the sides of the body. The phase indicates that these are fluctuating in-phase between $0.2 < z/H < 0.7$, and also across either side of the body. This observation suggests communication between the sides of the body. While frequencies of this magnitude were observed by Zhang et al. [41] and were attributed to the shedding off the front struts, our case presents a different view. Since the struts for the present study are in the centre-plane, away from the edges, and as the mode shape suggests, this frequency is due to the shear layer vortices.

3.3. Effects of aspect ratio

A similar cross-stream analysis was performed for the four varying-width bodies. The spatial average of the power spectra are given in Fig. 12 which shows the dominant peak changes only slightly with aspect ratio, from $St = 0.23$ for the 60% body to $St = 0.27$ for the 120% width. If these oscillations were driven by a von Kármán type instability from shedding from the side edges, the shedding frequency would be expected to scale linearly with the width. As a consequence, the body's height appears to be the dominant length scale and hence was used for non-dimensionalising the frequency.

The modes for the dominant oscillations are given in Fig. 13 with the first two rows corresponding to the power and phase distributions of v, followed by the power and phase distributions of w. The three widest bodies show similar characteristics in the mode shapes, specifically, they are symmetric in phase for v but anti-symmetric for w. The narrowest

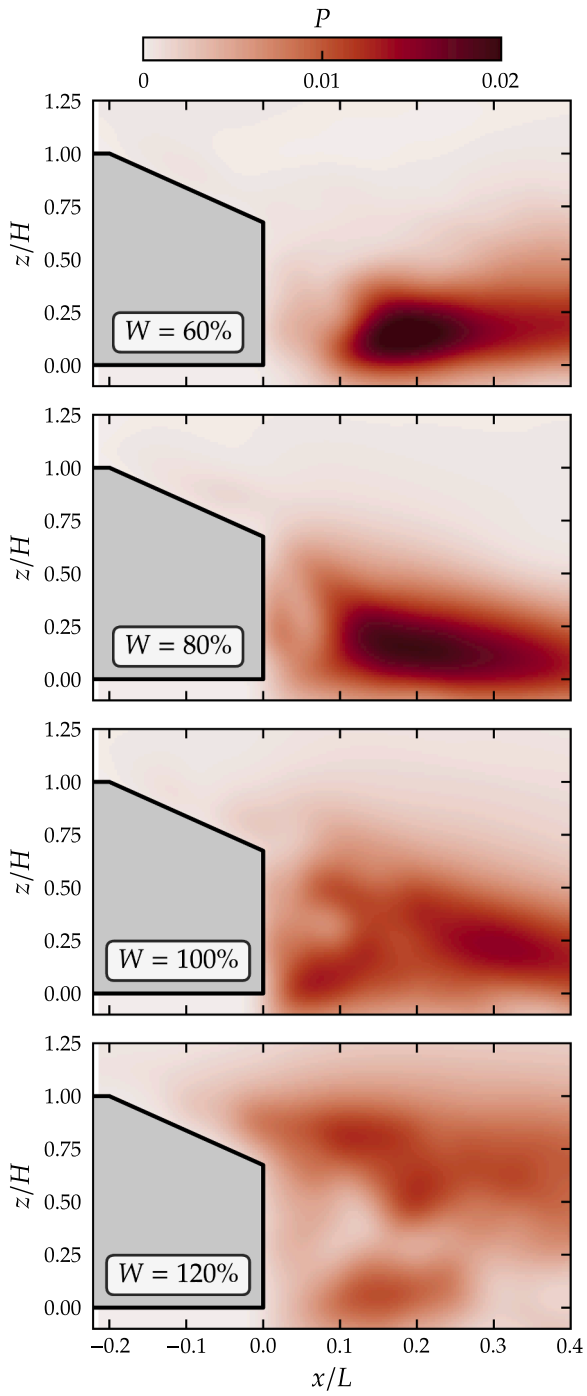

Fig. 16. Power of the vertical velocity fluctuations of the dominant frequency for each of the four bodies at $y/W = 0$. The intensity of the mode shape moves upward with increasing width.

case, however, shows the opposite situation: the spanwise serpentine mode is now a symmetrically-reflectant mode, ie. the velocity on both sides of the body moves outboards or inboards in-phase. This mode shift may be attributable to the fact that the 60% width body is the only geometry that is taller than it is wide, indicating that the symmetry plane of the dominant shedding mode is dictated by the orientation of the largest dimension.

While the differences in the cross-stream dynamics were minor except for the narrowest body, several differences were observed in the streamwise data, particularly in the motion of the A and B vortices, which are formed as the flow separates from the slant and base, respectively. For each instance in time, the core location of each vortex was extracted using the Γ_1 criteria. This data is presented as a two-dimensional histogram (by colour intensity) for each body tested in Fig. 14, and can be interpreted as the likelihood of the core being located at each position. Red indicates the location of the A-vortex, while the blue is the B-vortex.

For the narrowest body (60%), the upper A-vortex is moderately stable in time, reflecting a steady recirculatory vortex structure. The B-vortex location, however, is spread out over a longer, narrower downstream extent, indicating that this may be more similar to the shedding of shear-layer vortices than a standing vortex. Fig. 15 shows an instantaneous snapshot of the velocity field supporting this hypothesis.

For the 80% and 100% cases, the two vortices are tighter in spatial variation and closer to the body than the separated shear layers of the 60% and 120% bodies. This indicates the presence of two stable recirculation regions and the proximity to the body could indicate a higher drag coefficient (since the low pressure cores will be close to the body). The rear stagnation point between the two vortices tends to move upwards with increasing aspect ratio, corresponding to the weakening influence of the C-pillar vortices in maintaining the downwash [35].

For the widest case (120%), both vortices show higher scatter in their core location, indicating increased motion of the structures. The B-vortex is in a similar position to the 80% body, but the A-vortex is now spread along in the manner similar to that of a shear layer. As the body gets wider, the centre-plane flow becomes more like that behind a two-dimensional body, and the separated flow over the slant causes the A-vortex to be much weaker. Fig. 15 shows an instantaneous view of shear layer vortices emanating from the top of the slant, where the flow separates from the body.

The mode shape for the vertical component of the velocity is given in Fig. 16 for each geometry. For the narrowest body the intensity is close to the ground plane, downstream of the B-vortex. As the width increases, and the downwash is less effective at maintaining attached flow, the intensity of this region moves upward. At the widest body, the power distribution is concentrated in the separated shear layer behind the slant, but for each case there is still energy near $z/H = 0.1$, that is, behind the B-vortex.

4. Conclusions

The influence of the width of the Ahmed body on the dynamics of both large- and small-scale structures has been investigated using TR-PIV. A spectral decomposition reveals the motion of the vortical structures to be dominated by a transverse and vertical oscillation of the base-pressure region at $St = 0.24$ for the standard width body. This mode is symmetric in the spanwise velocity oscillations, and anti-symmetric in the vertical velocity oscillations, implying that the vortical structures are moving side-to-side, and the energy is concentrated below the C-pillar vortices. Interestingly, similar dynamics were identified by Bell et al. [6] in the wake of a high-speed train, suggesting that the phenomenon is somewhat insensitive to geometry. The shear-layer oscillations as the boundary layers separate from the sides of the body were observed in the near wake at a frequency of $St = 2.30$.

Four geometries were used with widths ranging from 60% to 120% of the standard Ahmed body geometry. Increasing the spacing between the C-pillar vortices reduced their influence to control the flow over the back slant. The shedding frequency of the principal motion of the vortical structures was only mildly dependent on the body width, and the modal analysis revealed a change in the shedding plane for the narrowest body. However, the top and bottom shear layers do vary according to the reattachment of the flow over the slant. For the narrowest case, there is an unsteady shear layer underneath the body, while the A vortex is stable due to the attached flow over the slant. For the widest case, the flow is separated over the entire slant, leading to a shear layer at the top, and a stable B vortex at the base. For the two intermediate widths, both A- and B-vortices are stable.

The elucidation of the dynamics of these large-scale wake structures provides some insight into the time-varying forces on the body. The distinct periodic movements of these vortices suggests that they may be effectively targeted by active flow control techniques, not only to alter the forces on the body, but also to minimise wake fluctuations which can reduce the impact of ground vehicles such as high-speed trains on the surrounding environment.

Declaration of Competing Interest

The authors declare that they have no known competing financial interests or personal relationships that could have appeared to influence the work reported in this paper.

Acknowledgements

The authors would like to acknowledge the financial support of the Australian Research Council (ARC) through Linkage Project LP0991170 and the Centre National de la Recherche Scientifique (CNRS) through Grant No. PICS161793 under the Projet International de Coopération Scientifique. TM acknowledges the support of an Australian Government Research Training Program Scholarship.

References

[1] Ahmed, S., Ramm, G., Faitin, G., 1984. Some salient features of the time-averaged ground vehicle wake. Tech. rep., Society of Automotive Engineers, Inc., Warrendale, PA.
[2] J.-L. Aider, J.-F. Beaudoin, J.E. Wesfreid, Drag and lift reduction of a 3d bluff-body using active vortex generators, Exp. Fluids 48 (5) (2010) 771–789.
[3] T. Avadiar, M. Thompson, J. Sheridan, D. Burton, The influence of reduced reynolds number on the wake of the drivaer estate vehicle, J. Wind Eng. Ind. Aerodyn. 188 (2019) 207–216.
[4] D. Barros, J. Borée, B. Noack, A. Spohn, T. Ruiz, Bluff body drag manipulation using pulsed jets and Coanda effect, J. Fluid Mech. 805 (2016) 422–459.
[5] J. Basley, L.R. Pastur, F. Lusseyran, T.M. Faure, N. Delprat, Experimental investigation of global structures in an incompressible cavity flow using time-resolved PIV, Exp. Fluids 50 (4) (2011) 905–918.
[6] J.R. Bell, D. Burton, M.C. Thompson, A. Herbst, J. Sheridan, Dynamics of trailing vortices in the wake of a generic high-speed train, J. Fluids Struct. 765 (2016) 238–256.
[7] Z. Carr, C. Chen, M. Ringuette, Finite-span rotating wings: three-dimensional vortex formation and variations with aspect ratio, Exp. Fluids 54 (2) (2013) 1444.
[8] M. Corallo, J. Sheridan, M.C. Thompson, Effect of Aspect Ratio on the Near-Wake Flow Structure of an Ahmed Body, J. Wind Eng. Ind. Aerodyn. (2015).
[9] U. Dallman, G. Schewe, On topological changes of separating flow structures at transition reynolds numbers, in: AIAA 19th Fluid Dynamics, Honolulu, USA, 1987.
[10] Drouin, V., Giovannini, A., Gilliéron, P., 2002. Topology and characterisation of the vortical near-wake flow over a simplified car model. In: Conference on Bluff Body Wakes and Vortex-Induced Vibrations (BBVIV3). pp. 1–4.
[11] B.P. Epps, A.H. Techet, An error threshold criterion for singular value decomposition modes extracted from piv data, Exp. Fluids 48 (2) (2010) 355–367.
[12] J.N. Fernando, D.E. Rival, On vortex evolution in the wake of axisymmetric and non-axisymmetric low-aspect-ratio accelerating plates, Phys. Fluids 28 (1) (2016) 017102.
[13] A. Fouras, D. Lo Jacono, K. Hourigan, Target-free Stereo PIV: a novel technique with inherent error estimation and improved accuracy, Exp. Fluids 44 (2) (2007) 317–329. Oct.
[14] Graftieaux, L., 2001. Combining PIV, POD and vortex identification algorithms for the study of unsteady turbulent swirling flows. Measurement Science and Technology 1422.
[15] M. Grandemange, M. Gohlke, O. Cadot, Bi-stability in the turbulent wake past parallelepiped bodies with various aspect ratios and wall effects, Phys. Fluids 25 (9) (2013) 095103.
[16] M. Grandemange, M. Gohlke, O. Cadot, Turbulent wake past a three-dimensional blunt body. Part 1. Global modes and bi-stability, J. Fluid Mech. 722 (2013) 51–84.
[17] M. Grandemange, M. Gohlke, O. Cadot, Turbulent wake past a three-dimensional blunt body. part 2. experimental sensitivity analysis, J. Fluid Mech. 752 (2014) 439–461.
[18] R.R. Harbig, J. Sheridan, M.C. Thompson, Reynolds number and aspect ratio effects on the leading-edge vortex for rotating insect wing planforms, J. Fluid Mech. 717 (2013) 166–192.
[19] Y. Huang, J. Venning, M.C. Thompson, J. Sheridan, Vortex separation and interaction in the wake of inclined trapezoidal plates, J. Fluid Mech. (2015) 1–26.
[20] P. Joseph, X. Amandolèse, J.L. Aider, Drag reduction on the 25 slant angle Ahmed reference body using pulsed jets, Exp. Fluids 52 (5) (2012) 1169–1185.
[21] S. Krajnović, L. Davidson, Flow Around a Simplified Car, Part 1: Large Eddy Simulation, J. Fluids Eng. 127 (5) (2005) 907.
[22] J. Mcnally, E. Fernandez, R. Kumar, F. Alvi, S. Number, Near Wake Dynamics for an Ahmed Body with Active Flow Control, in: 6th AIAA Flow Control Conference, 2012, pp. 1–11.
[23] M. Minguez, R. Pasquetti, E. Serre, High-order large-eddy simulation of flow over the Ahmed body car model, Phys. Fluids 20 (9) (2008).
[24] A. Nemes, D.L. Jacono, H.M. Blackburn, J. Sheridan, Mutual inductance of two helical vortices, J. Fluid Mech. 774 (2015) 298–310.
[25] Okada, M., 2006. Experimental investigations of wake flow structures behind simplified automotive geometries, Ph.D. thesis, Monash University.
[26] G. Pavia, M. Passmore, M. Varney, Low-frequency wake dynamics for a square-back vehicle with side trailing edge tapers, J. Wind Eng. Ind. Aerodyn. 184 (2019) 417–435.
[27] A. Rao, G. Minelli, B. Basara, S. Krajnović, On the two flow states in the wake of a hatchback ahmed body, J. Wind Eng. Ind. Aerodyn. 173 (2018) 262–278.
[28] K. Taira, T. Colonius, Three-dimensional flows around low-aspect-ratio flat-plate wings at low Reynolds numbers, J. Fluid Mech. 623 (2009) 187. Mar.
[29] A. Thacker, S. Aubrun, A. Leroy, P. Devinant, Unsteady analyses of the flow separation on the rear window of a simplified ground vehicle model, in: In: 28th AIAA Applied Aerodynamics Conference, Chicago, 2010, pp. 1–11.
[30] A. Thacker, S. Aubrun, a. Leroy, P. Devinant, Experimental characterization of flow unsteadiness in the centerline plane of an Ahmed body rear slant, Exp. Fluids 54 (3) (2013).
[31] A. Towne, O.T. Schmidt, T. Colonius, Spectral proper orthogonal decomposition and its relationship to dynamic mode decomposition and resolvent analysis, J. Fluid Mech. 847 (2018) 821–867.
[32] T. Tunay, B. Sahin, V. Ozbolat, Effects of rear slant angles on the flow characteristics of Ahmed body, Exp. Thermal Fluid Sci. 57 (2014) 165–176.
[33] E. Varon, J.-L. Aider, Y. Eulalie, S. Edwige, P. Gilotte, Adaptive control of the dynamics of a fully turbulent bimodal wake using real-time piv, Exp. Fluids 60 (8) (2019) 124.
[34] J. Venning, Vortex structures in the wakes of two- and three-dimensional bodies, Ph.D. thesis, Monash University, 2016.
[35] J. Venning, D. Lo Jacono, D. Burton, M. Thompson, J. Sheridan, The effect of aspect ratio on the wake of the Ahmed body, Exp. Fluids 56 (6) (2015).
[36] Venning, J., Lo Jacono, D., Burton, D., Thompson, M.C., Sheridan, J., 2017. The nature of the A and B vortical structures in the wake of the Ahmed body. IMECHE Part D.
[37] G. Vino, S. Watkins, P. Mousley, J. Watmuff, S. Prasad, Flow structures in the near-wake of the Ahmed model, J. Fluids Struct. 20 (5) (Jul. 2005) 673–695.
[38] R. Volpe, P. Devinant, A. Kourta, Unsteady experimental characterisation of the natural wake of a squareback Ahmed model, in: Proceedings of the ASME 2014 4th Joint US-European Fluids Engineering Division Summer Meeting, Chicago, USA, 2014, pp. 1–9.
[39] R. Volpe, P. Devinant, A. Kourta, Experimental characterization of the unsteady natural wake of the full-scale square back Ahmed body: flow bi-stability and spectral analysis, Exp. Fluids 56 (5) (2015) 1–22.
[40] X.W. Wang, Y. Zhou, Y.F. Pin, T.L. Chan, Turbulent near wake of an Ahmed vehicle model, Exp. Fluids 54 (4) (2013).
[41] B.F. Zhang, Y. Zhou, S. To, Unsteady flow structures around a high-drag Ahmed body, J. Fluid Mech. 777 (2015) 291–326.